

Analytical and Experimental Evaluation of Aerodynamic Thrust Vectoring on an Aerospike Nozzle

Journal:	<i>Joint Propulsion & International Energy Conversion Engineering Conferences</i>
Manuscript ID:	Draft
Conference:	Joint Propulsion Conference
Date Submitted by the Author:	n/a
Contact Author:	Whitmore, Stephen; Utah State University, MAE



Manuscript Only

Analytical and Experimental Evaluation of Aerodynamic Thrust Vectoring on an Aerospike Nozzle

Shannon D. Eilers¹, Matthew D. Wilson¹ and Stephen A. Whitmore²
Utah State University, Logan, Utah, 84322

Results from analytical and experimental investigations of aerodynamic thrust vectoring on a small-scale aerospike thruster are presented. The thrust vectoring system uses four secondary injection ports located at approximately 50% of the nozzle length. The nozzle was truncated at 57% of its theoretical length to enhance manufacturability. The resulting low-pressure base-area decreases overall thrust levels, and this effect is partially compensated-for by injecting mass from the nozzle base area. Two-dimensional method-of-characteristics techniques were used to size the system, and allowed calculation of the desired nozzle contours. CFD computations verified the method-of-characteristics solutions, and were used to visualize the associated secondary injection flow phenomena. Analytical calculations are correlated with experimental data measured with a custom-designed 6-degree-of-freedom thrust stand. In-situ calibration procedures for the thrust stand are presented. Data derived from cold-flow thrust vectoring tests with carbon dioxide as the working fluid are presented. These data demonstrate that the injected secondary flow pulses produce substantial side forces. These forces crisply reproduce input pulses with a high degree of fidelity. The achieved side force levels are approximately 1.5% of the total thrust level. Cold flow-tests do not verify existence of an aerodynamic multiplying effect on the generated impulsive side force.

Nomenclature

A^*	=	plenum exit throat area, cm^2
D_{exit}	=	plenum exit outer diameter, cm
D_{plug}	=	aerospike plug maximum, cm
D_{throat}	=	plenum exit throat hydraulic diameter, cm
\tilde{F}	=	matrix of calibration inputs, N or $N-m$
F_x	=	axial thrust load, N
F_y	=	lateral thrust load, N
F_z	=	normal thrust load, N
g_0	=	standard gravitational acceleration, $9.8067 m/s^2$
I_{sp}	=	specific impulse, s
$\{I\}$	=	load cell index
$I_{sp\ axial}$	=	main flow specific impulse, s
$I_{sp\ sf}$	=	side force specific impulse, s
J	=	thrust stand Jacobian matrix, $N/volt$ or $N-m/volt$
\hat{J}	=	least squares estimate of thrust stand calibration matrix, $N/volt$ or $N-m/volt$
L	=	truncated spike length, cm
L_{isen}	=	isentropic plug length, cm
M_{exit}	=	nozzle exit plane Mach number

¹ Graduate Research Assistant, Mechanical and Aerospace Engineering (MAE) Department, 4130 Old Main Hill, Logan, Utah, 84322-4130, AIAA Student Member.

² Assistant Professor, Mechanical and Aerospace Engineering (MAE) Department, 4130 Old Main Hill, Logan, Utah, 84322-4130, AIAA Member.

1		
2		
3	MSL	= mean sea level altitude, m
4	\dot{m}_{plenum}	= plenum mass flow, kg/s
5	$\dot{m}_{\text{secondary injection}}$	= secondary injection mass flow, kg/s
6		
7		
8	N	= number of thrust stand calibration data sets
9		
10	$S_{\bar{x}}$	= calibration confidence interval, N or $N-m$
11	t_{95}	= student t variable corresponding to 0.95 double sided probability level
12	T	= thrust, N
13		
14	q	= pitch rate, deg/s
15	$r(x)$	= radial distance from nozzle spike axial centerline, cm
16	\tilde{V}	= matrix of calibration outputs, $volts$
17	V_{Aa}	= voltage reading from axial load cell "A", $volts$
18	V_{Ba}	= voltage reading from axial load cell "B", $volts$
19	V_{Ca}	= voltage reading from axial load cell "C", $volts$
20		
21	V_{Al}	= voltage reading from lateral load cell "A", $volts$
22	V_{Bl}	= voltage reading from lateral load cell "B", $volts$
23	V_{Cl}	= voltage reading from lateral load cell "C", $volts$
24		
25	$V_{I I_{adj}}$	= adjusted lateral load cell reading, $mVolt$
26		
27	x	= longitudinal coordinate, m
28	y	= lateral coordinate, m
29	z	= lateral coordinate, m
30		
31	ε	= nozzle expansion ratio
32	η_{trun}	= spike truncation ratio, %
33	$\hat{\sigma}_x$	= sample standard deviation, N or $N-m$
34		
35	$\frac{\partial F_i}{\partial V_j}$	= variation of force from load cell "i" with respect to sensed voltage "j", $volts/N$
36		
37	$\frac{\partial M_j}{\partial V_i}$	= variation of moment from load cell "i" with respect to sensed voltage "j", $volts/N-m$
38		
39	$()^T$	= matrix transpose
40		
41		

I. Introduction

Achieving the large range of human and robotic space exploration missions outlined in NASA's national space vision will require significant advances in technology from all systems of a space vehicle, especially propulsion systems. Advances in propulsion technologies offer the greatest potential for spacecraft mass reduction. Mass reductions are especially critical for planetary landing and ascent propulsive systems like those proposed for the Mars Ascent Vehicle¹ or the Altair Lunar Lander where the cost of delivering mass to the surface is so high.

While *aerospike nozzles* have long been known for their altitude compensation ability during endo-atmospheric flight, they also present significant potential advantages for purely in-space applications. Aerospike nozzles can be both more efficient and significantly smaller than conventional high expansion ratio bell nozzles. Given a fixed vehicle base area, an aerospike nozzle can present higher area expansion ratio than a bell nozzle, providing better performance in a space environment or near vacuum environment like Mars. The increased specific impulse (I_{sp}) due to a higher possible expansion ratio using an aerospike nozzle translates to a 8-9% decrease in the propellant mass and total system weight for space and near-space applications². Additionally, one of the often-overlooked properties of the aerospike nozzle is the ability to achieve thrust vectoring *aerodynamically* without active mechanical nozzle gimbals, which offers a significant potential for reduced system complexity and weight.

Figure 1 compares two aerospike-based nozzle designs to their conventional counterparts with the same effective expansion ratios. Fig 1a compares the original Saturn V first stage F-1A engine to its proposed replacement J-2T-250K aerospike engine (featuring a truncated plug nozzle).³ It should be noted that both of these engines are optimized for earth atmospheric conditions. At Mars and vacuum conditions, the size difference is more pronounced. This size difference is illustrated by Fig. 1b where the proposed 12.1 kNt Altair Lander Engine is compared to its aerospike equivalent. In both examples, the size differences are dramatic.⁴

Despite these potential benefits over conventional conical or bell-nozzle designs, because of a perceived low technology readiness level (*TRL*) the aerospike rocket configuration has never been deployed on an operational space vehicle. One of the major reasons for this perception is the lack of high quality ground and flight test data and its correlation with analytical flow predictions. This dearth of data is especially true with regard to off-nominal design performance, thrust vectoring, and thruster-out scenarios for clustered aerospike configurations.

The analytical and experimental work outlined in this paper will fill in the “gaps” in the experimental data chain. A primary experimental emphasis is to develop methods for using the aerospike nozzle for aerodynamic thrust vectoring. Redundancy management and off-design performance issues will also be addressed. The goal is a rapid upgrade of the systems technology to level 4 within a year, and an eventual upgrade to *TRL* 6 by the end of the proposed three-year research period. Such an upgrade in the *TRL*-level would make the aerospike design competitive with conventional nozzle designs, and will enable aerospike-based propulsion systems to be considered as a valid flight design option for future space vehicle designs.

II. Experimental Approach and Methodology

The experimental work described by this paper will progress from cold jet testing in a laboratory environment (Spring/Summer 2010), to vacuum-chamber testing (Winter 2011), and then to hot-gas aerospike system testing (Summer 2011/Winter 2012). Within each phase, comprehensive high fidelity data sets will be obtained and will be compared with a variety of analytical models for corresponding nozzle shapes and flow conditions. Following the completion of the ground-based experimental tests, it is anticipated that the developed nozzle design can be adapted for a flight test article.

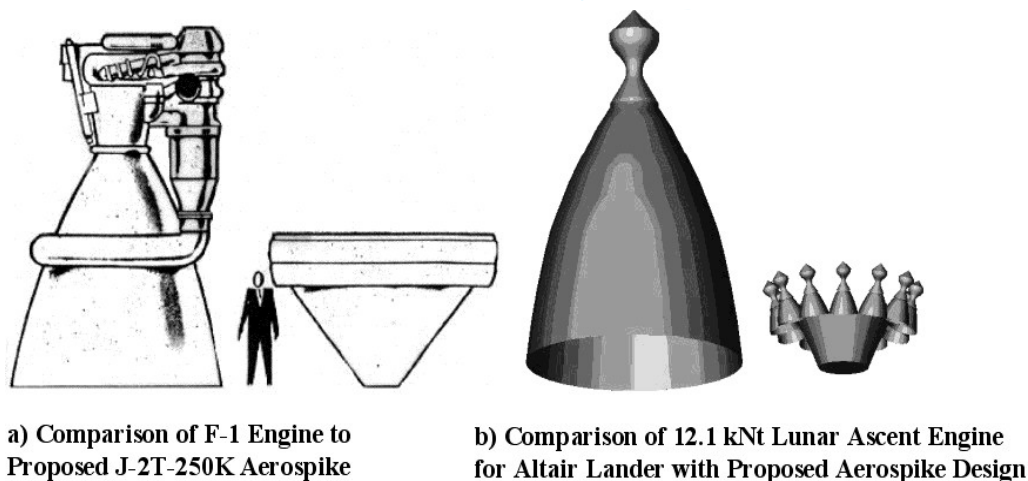


Figure 1. Conventional nozzles compared to equivalent aerospike configurations.

A primary emphasis of the ground-based experimentation is to develop methods for aerospike nozzle thrust vectoring control (*TVC*). Redundancy management and performance issues will also be addressed. Hypotheses to be investigated during the experimental work include:

- i) Does aerodynamic flow manipulation have “response fidelity” that is controllable and repeatable?
- ii) What is the limit of the effective vectoring moment coefficient, and what are the corresponding mass flow requirements?
- iii) What is the characterizable vectoring “bandwidth”?
- iv) How does one perform redundancy management for damaged flow paths and injector or inlet “thruster out” scenarios?
- v) How does plug truncation and off-design operation affect vectoring effectiveness?
- vi) What is the impact of TVC and engine-out scenarios to overall engine thrust and I_{sp} ?

The fluid mechanics of aerodynamic thrust vectoring on a small scale aerospike nozzle has been the primary focus of the year 1 investigation. Both analytical and experimental investigations have been performed. A 6-degree-of-freedom test cell has been designed, fabricated, integrated, calibrated, and used to generate preliminary test data. A series of CFD calculations have been performed, and will be compared with test stand results. This report will detail the results of 4 aspects of the research program: (1) Aerospike nozzle surface contour and sizing calculations, (2) CFD analysis, (3) Test stand design and calibration; and finally (4) Preliminary cold-gas test results. Extensive comparisons of the analytical and test results will be deferred to year 2 of this research.

III. Nozzle Surface Contour and Sizing Calculations

For the first phase of testing, cold flow tests benchmark the effectiveness and fidelity of aerodynamic thrust vectoring. For high measurement fidelity, axial loads between 200 to 400 Newtons with vectoring side forces approximately an order of magnitude lower are desired. However, for low specific impulses achieved by cold-gas thrusters, even these modest thrust ranges require a high mass flow rate that can be difficult to reach with commercial off-the-shelf (COTS) components. To be cost and schedule feasible, the aerospike nozzle itself needs to be of reasonable size so that components can be constructed using conventional machining techniques. Finally, since the primary focus of this research is aerodynamic thrust vectoring for application in high altitude or space applications, the flow field generated on the test aerospike nozzle must be similar to one generated by an optimally expanded space nozzle. These considerations result in a multi-parameter design space.

One of the most important design constraints is the system mass flow. For a cold-gas system, the fluidic component cost and sizing grow almost exponentially with increasing mass flow requirements. To examine the tradeoffs associated with the aerospike design, and to size the system for thrust and mass flow levels that are achievable, a parametric study was conducted using conventional inviscid, axi-symmetric compressible fluid mechanics techniques. Figure 2 shows the geometrical layout. Here, the design features a sonic, annular throat with an annular plenum feeding the throat. The nozzle expands along an isentropic contour line at the design altitude. A USU-developed method-of-characteristics⁵ code, based upon the methods of Lee and Thompson⁶ was used to calculate these isentropic contour lines.

In order to test the effectiveness of aerodynamic thrust vectoring for space or high-altitude conditions, it is important that the experimental nozzle produce a flow field with pressure contours on the nozzle surface that are similar to those that occur under space-like conditions. At the sonic outlet of the aerospike plenum, a series of expansion waves propagate toward the plug from the outer lip of the chamber cowl toward the plug surface contour. These expansion waves impinge on the aerospike plug, reflect outwards toward the free boundary, and then re-reflect from the free external flow boundary as compression waves. For optimal or under-expanded operating conditions, these reflected compression waves propagate sufficiently downstream so as not to impinge on the plug surface. The result is a nozzle that is loss free along the surface contour. This case typically occurs when an aerospike nozzle is operated in vacuum conditions.

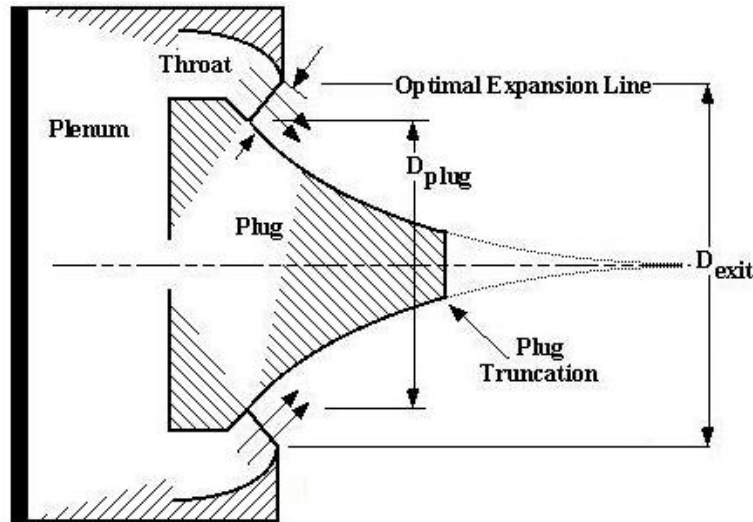


Figure 2. Baseline configuration for aerospike plenum and nozzle.

For a ground-based test operating at near-ambient conditions, a nozzle designed for space operation will be significantly over-expanded. For over-expanded conditions, the free-stream boundary contracts toward the plug and the reflected compression waves impinge on the spike. The result is an oblique shock wave that produces a sharp rise in pressure and corresponding drop in Mach number. This effect is especially prevalent near the aft end of the plug. More importantly, the entropy increase across the shock wave causes a loss in total pressure and reduced the overall efficiency of the nozzle. Thus, for this experiment, the nozzle plug must be optimally expanded, under-expanded, or over-expanded but truncated so that the compression waves impinge aft of the physical spike surface.

To visualize the design space, parametric curves were generated for nozzles optimized for the altitude of Logan, Utah -- approximately 1360 meters above mean sea level, and for nozzles over-expanded by a ratio of 0.5 and 1.0. Under-expanded nozzles, because they do not represent an in-space configuration, were not investigated. For this design the plenum (chamber) pressure, P_0 and outer throat annulus diameter, D_{exit} are keys to sizing the system mass flow and thrust level, and were selected as independent variables for the parametric study. Using the method of characteristics code, and one-dimensional, inviscid, isentropic fluid relationships (Ref. 5, Chapter (3)), the resulting thrust, mass flow rate, throat area, and plug diameter were calculated. The throat area is the area of the annulus between D_{exit} and D_{plug} . The expansion ratio (ϵ) of the nozzle is defined as the ratio of the area swept out by the exit radius about the nozzle centerline, $\pi D_{exit}^2/4$, and the area of the throat annulus.

The results of these calculations are presented in Figures 3-6. In these figures the contours for thrust are color coded, and the contours for mass flow and plug diameter are shown as dashed lines. Figure 3a shows the parametric curves for a nozzle optimized for Logan UT, which is at approximately 1362 MSL. The optimal ϵ is plotted as a function of chamber pressure ratio in Fig. 3b. At a chamber pressure of a 1000 kPa (145 psia) the optimal ϵ is approximately 2.1 for 1362 m MSL altitude. Figure 4 plots the same data, but now the nozzle has been over-expanded by an additional 0.5 in ϵ . Finally, Fig. 5 plots the parametric curves for a nozzle over-expanded by an additional 1.0 in ϵ . In these calculations carbon-dioxide (CO_2) was used as the working fluid.

As mentioned earlier, the cost of the system components goes up almost exponentially as the mass flow of the system is increased. A brief trade study looking at available COTS industrial flow regulators demonstrated that the most cost effective mass flow range (cost/per delivered thrust) would lie in the region between 0.5 and 1.5 kg/sec mass flow. The regulator selected for the project allows a maximum mass flow rate of 1.4 kg/sec and has a nominal operating range of 690 kPa. Based on the data presented in Figures 4-6 a plug diameter (D_{plug}) in the range of 2.5 to 3.5 cm produces a mass flow rate that varies from 0.5 to 1.5 kg/sec at an operating pressure of 690 kPa MP.

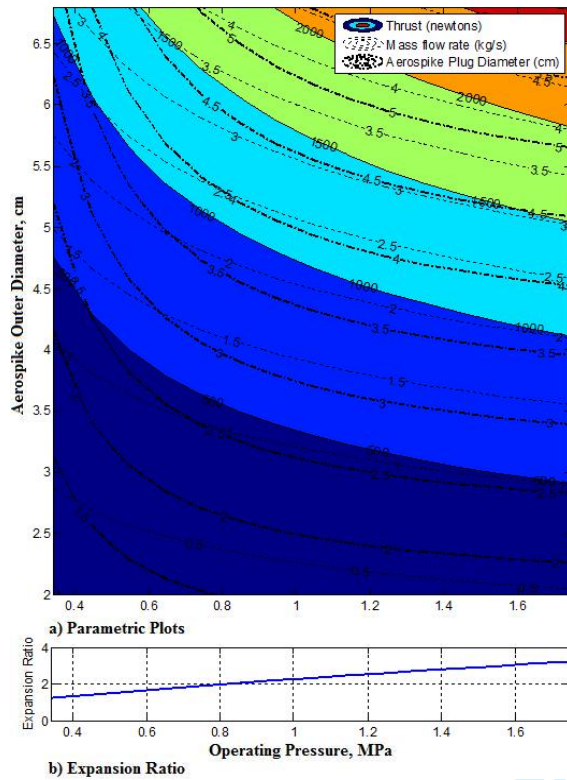


Figure 3. Parametric curves for aerospike nozzle optimized for 1362 m MSL altitude.

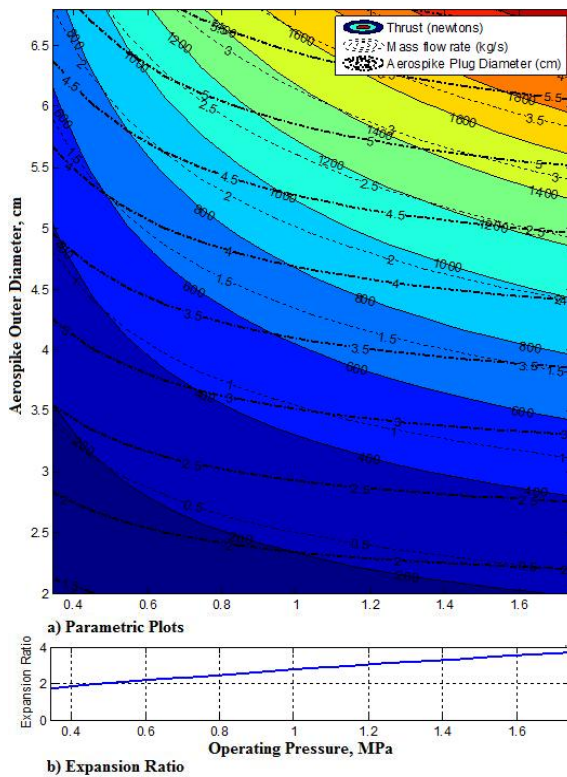


Figure 4. Parametric curves for aerospike nozzle at 1362 m MSL optimal + 0.5 ϵ .

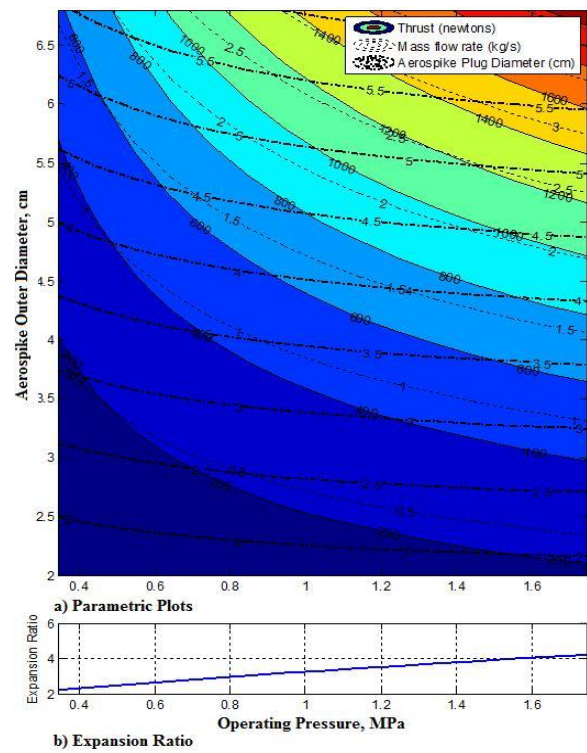


Figure 5. Parametric curves for aerospike nozzle at 1362 m MSL optimal + 1.0 ϵ .

Although a plug designed to be under-expanded or optimally expanded at local pressures closely approximates an in-space thruster, lower ε nozzles require larger flow rates or smaller spikes; neither alternative was deemed acceptable. Thus, a higher-than-optimum ε was favored for the project. In order to ensure that reflected compression waves do not reach the end of the spike, the spike was truncated short of its ideal ε .

A. Size Verification Using Method of Characteristics and Fluent® CFD Solutions

To verify the results of the parametric study, three of the suggested configurations were analyzed using both the USU-developed *method of characteristics* (Ref. 5) code and a commercially distributed *computational fluid dynamics* (CFD) solver, ANSYS FLUENT.⁷ The nozzle contours analyzed corresponded to (1) *optimal* ε for 1362 MSL altitude with an operating pressure of 775 kPa, (2) a nozzle over-expanded by *optimal* + 0.5 ε , and (3) a nozzle over-expanded by *optimal* + 1.0 ε . As with the preliminary sizing calculations, carbon-dioxide (CO₂) was used as the working fluid.

The results of both computational studies showed that when the spike was truncated at $\eta_{trun}=75\%$ of its theoretically optimal length, the compression waves reflected from the outer flow boundary do not impinge on the *optimal* + 0.5 ε nozzle. As the optimally expanded nozzle's small size would have created manufacturing difficulties, a truncated nozzle over expanded by *optimal* + 0.5 ε was chosen for the test article. The actual design altitude where this nozzle would perform optimally is approximately 4210 m above MSL for a chamber pressure of 775 kPa and 300 K temperature. Table 1 lists the final design parameters. The base area of the $\eta_{trun} = 75\%$ nozzle was so small that it was difficult to insert a base bleed port and still have sufficient material remaining to provide structural integrity. As a compromise the actual nozzle was truncated at $\eta_{trun} = 57\%$ of its theoretical isentropic length. This slightly shorter length was chosen to simplify manufacturing and still retain good overall performance.

Table 1. Final aerospike design parameters.

Aerospike Parameter	Value
Plug Diameter, D_{plug}	3.20 cm
Outer Plenum Diameter, D_{exit}	3.86 cm
Truncated Length, L	2.54 cm
Isentropic Spike Length, L_{isen}	4.31 cm
Truncation Ratio, η_{trun}	57%
Throat Diameter, D_{throat}	0.29 cm
Operating Stagnation Pressure, P_0	775 kPa (112.5 psia)
Nozzle Expansion Ratio, ε	2.47
Plenum Exit Throat Area, A^*	4.73 cm ²
Secondary Injection Port Diameter	0.3175 cm
Design Altitude	4210 m MSL
Design Thrust (300 K plenum temperature)	454 N

1. Method of Characteristics Solutions

Figure 6 plots the spike surface contour derived from the method of characteristics analysis. The 57% and 75% truncation points are shown along with the plenum exit stream lines for the operating (1360 m MSL) and the design (4210 m MSL) altitudes. The plenum throat exit is also labeled. For the $\eta_{trun} = 57\%$ nozzle, the operating altitude (1360 m MSL), with a plenum pressure of 775 kPa and temperature of 300 K, the predicted thrust level is approximately 454 Newtons, and the mass flow is 1.02 kg/sec. For the same nozzle at the experimentally measured chamber temperature (255 K), the mass flow rate is approximately 1.11 kg/s and the predicted thrust is approximately 422.7 N. At the design altitude (4210 m MSL) for these conditions the thrust would be 478.0 Newtons. When the nozzle is lengthened to $\eta_{trun} = 75\%$, the operating and optimal thrust levels increase to 454.3 N and 481.3 N respectively. This result, with a performance decrease of approximately 6%, verifies the earlier assumption that the performance differences between the 57% and 75% nozzle truncations would be minimal.

Table 2 summarizes the method of characteristics results. The assumed mean gas temperature in the plenum is 255 K. The parameter M_{exit} , is defined as the mean Mach number at the exit plane of the spike truncation point.

Calculations for two different plenum pressures, 600 kPa and 775 kPa are presented. When the plenum pressure is reduced to 600 kPa, all of the thrust and mass flow numbers drop by approximately 20%.

Table 2. Summary of method of characteristic calculations, 2.47 expansion ratio.

Operating Altitude	Plenum Pressure								
	600 kPa (6110 m MSL Design Altitude)				775 kPa (4210 m MSL Design Altitude)				
57% Truncation									
1362 m	<i>Thrust, N</i>	<i>m_{plenum}, kg/s</i>	<i>M_{exit}</i>	<i>I_{sp}, s</i>	<i>Thrust, N</i>	<i>m_{plenum}, kg/s</i>	<i>M_{exit}</i>	<i>I_{sp}, s</i>	
	311.1	0.858	1.78	36.97	422.7	1.108	1.91	38.89	
Design Altitude	347.7	0.858	2.10	41.32	478.0	1.108	2.12	43.79	
75% Truncation									
1362 m	<i>Thrust, N</i>	<i>m_{plenum}, kg/s</i>	<i>M_{exit}</i>	<i>I_{sp}, s</i>	<i>Thrust, N</i>	<i>m_{plenum}, kg/s</i>	<i>M_{exit}</i>	<i>I_{sp}, s</i>	
	324.4	0.858	1.86	38.55	454.3	1.108	2.10	41.80	
Design Altitude	361.4	0.858	2.20	42.94	481.3	1.108	2.31	44.29	

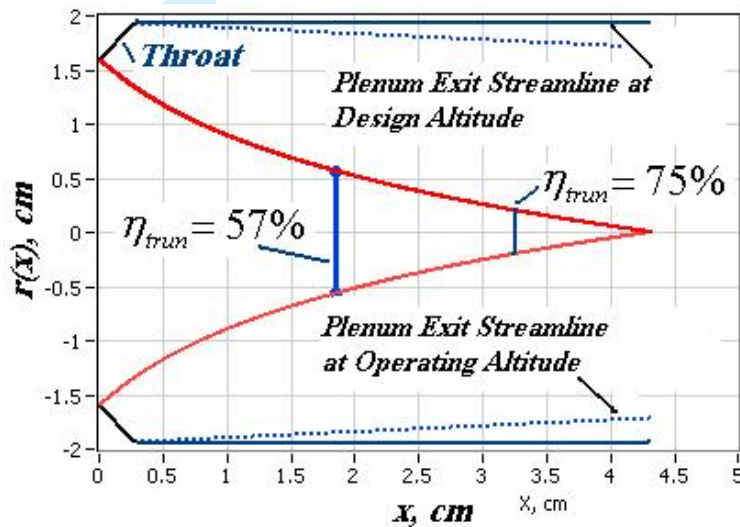


Figure 6. Aerospike contour from method of characteristics analysis, $P_0 = 775$ kPa.

2. CFD Verification

Computational fluid dynamics solutions using compressible Reynolds Averaged Navier Stokes Equations were created as a cross validation for the previously described method of characteristics results and to provide a stepping point for following asymmetric CFD results for thrust vectoring. Table 3 shows results for both the method of characteristics and CFD for the design inlet temperature of 300 K and a chamber pressure of 775 kPa. The static pressure along the spike contour as a function of radial location is shown in Fig. 7. Both sets of results show good agreement. The divergence between the CFD and method of characteristics derived pressures occur near the throat where the method of characteristics code idealizes the flow angle and near the axis where the straight characteristics lines assumed by the method of characteristics code also begin to break down.

Figure 8 shows the CFD-derived Mach number contours for this configuration. The plotted contours are the local flow Mach number with warm colors representing higher Mach numbers and cold colors representing low Mach numbers. The reflected compression waves are clearly visible. These compression waves do not impinge upon the aerospike surface for the 57 % truncated spike. This yields the desired generally monotonically decreasing pressure profile similar to what would be seen on a space thruster.

Table 3. CFD Results and Method of Characteristics Comparison

Result	Method of Characteristics	CFD	Difference
Total Thrust	454 N	446 N	2.0%
Exit Velocity	444.3 m/s	437.4 m/s	1.6%
Mass Flow Rate	1.022 kg/s	1.017 kg/s	0.5%
Specific Impulse	45.3 s	44.7 s	1.3%

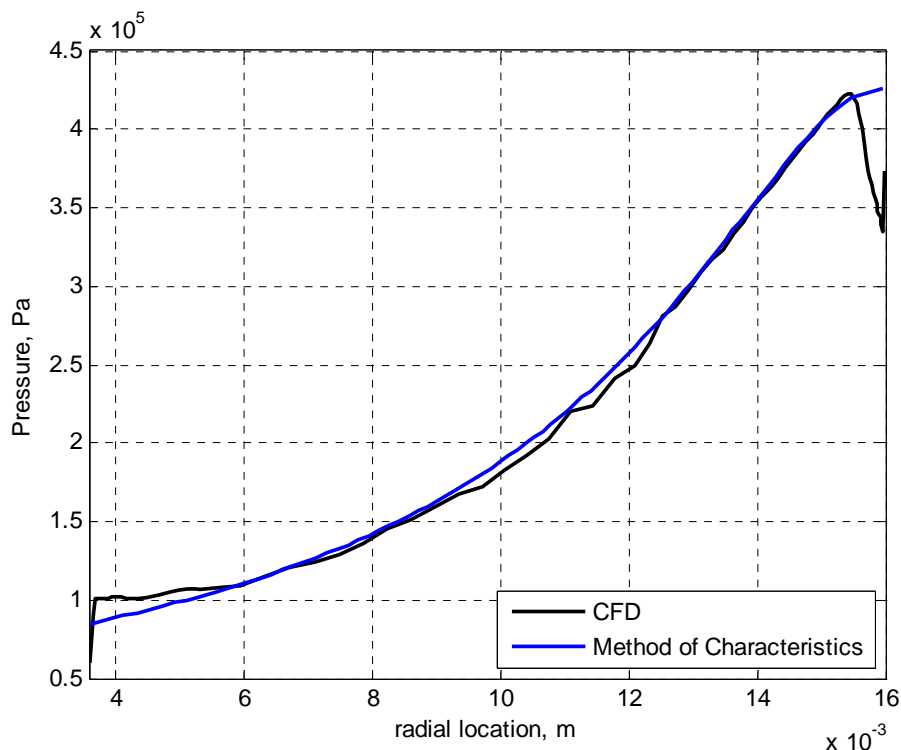


Figure 7. Comparison Aerospike surface pressure as a function of radial distance from centerline for CFD and method of characteristics.

B. Description of the Initial Test Article.

Figure 9a presents a 3-D solid model of the aerospike test article resulting from the sizing and CFD verification analyses presented in the previous sections. Figure 9b shows one of the fabricated test articles. Features including the plenum exit, thrust vectoring injection ports, spike contour, and base bleed are shown. The coin (a Jefferson Dollar) in the image illustrates the scale. The aerospike assembly consists of three pieces, the aerospike plug and two structures that form the walls of the plenum and the outer edge of the annular throat around the aerospike. The lower piece interfaces with fluid feed line hoses and a six degree of freedom thrust stand. The plenum is formed into four chambers that allow cross flow between chambers for pressure equalization, but are designed to be separately sealed to facilitate differential plenum thrust vectoring.

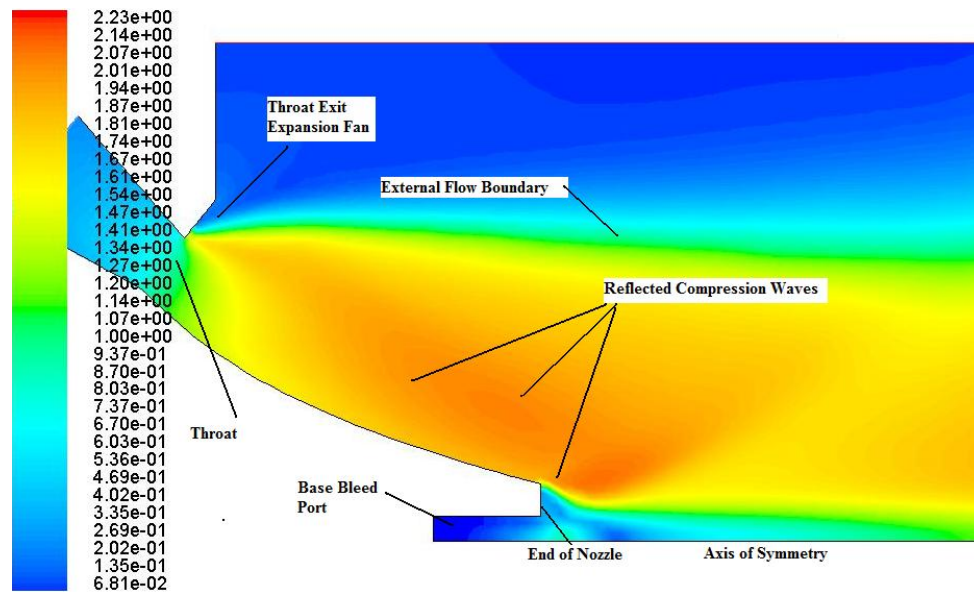
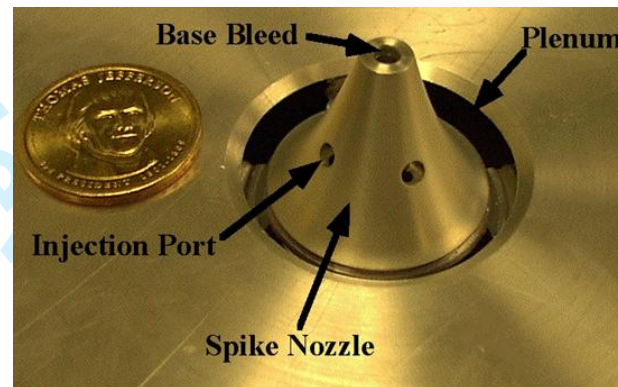
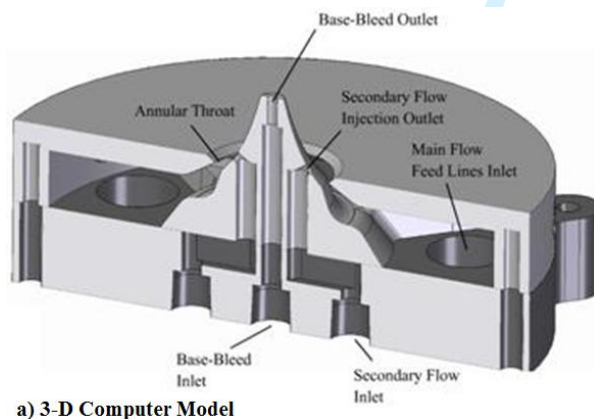


Figure 8. CFD-Derived Mach number contours for final aerospike configuration.



a) 3-D Computer Model

b) Prototype Plenum, Aerospike Nozzle and Injection Ports

Figure 9. Design and prototype for laboratory-scale aerospike nozzle and plenum.

IV. Preliminary CFD Analysis

A. CFD Analysis of Thrust Vectoring through Gas Injection

Figure 10 and Figure 11 present CFD solutions illustrating the flow-injection thrust-vectoring concept performed by the authors of this report. The CFD analyses provide a preliminary description of the interaction flow phenomenon. These data guided the initial inlet port geometry and placement. The plotted contours are the local flow Mach number with warm colors representing higher Mach numbers and cold colors representing low Mach numbers. Flow field data presented here illustrate the fluid mechanisms that produce the lateral forces on the spike wall. Figure 10 shows an axi-symmetric spike design with 4 injection ports placed circumferentially at right angles around the spike. Figure 11 illustrates what happens to the flow downstream of the injection point when a 775 kPa gas-pulse is injected into the main flow.

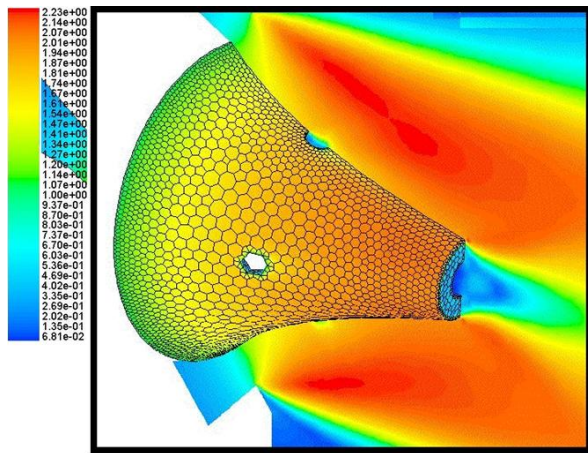


Figure 10. Aerospike surface Mach-number contours without flow injection.

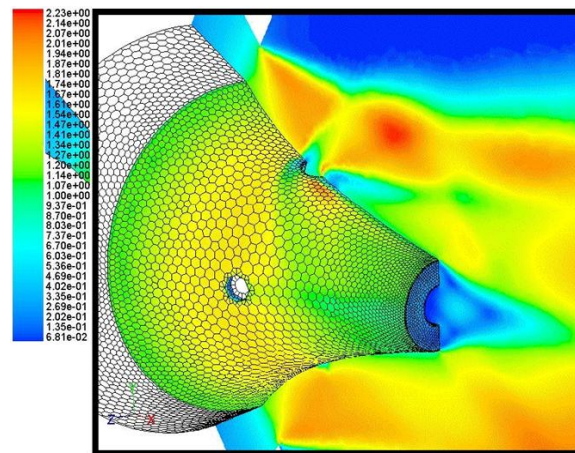


Figure 11. Aerospike surface Mach-number contours with flow injection.

The thrust vectoring force mechanisms for cold flow injection are similar to those involved in hot flow thrust vectoring in bell nozzles, however, due to the convex shape of an aerospike surface, the net forces generated by these mechanisms are different from those encountered in a bell nozzle. For hot gas injection in conventional bell nozzles the primary side force amplification phenomenon is generated by flow separation and a resulting bow shock just before the injection port. This increases the local pressure on the nozzle surface, resulting in an effect that amplifies the thrust generated by the momentum of the secondary flow. Downstream of the injection port there is a low pressure region created by the overexpansion of the injected fluid and a high pressure region created by the continuation of the aforementioned bow shock. In a bell nozzle, the flow effects downstream of the injection port tend to cancel out, and the previously described amplification effect is then predominant.⁸ However, due to the convex shape of an aerospike nozzle the effects of the bow shock are diminished downstream of the injection point leaving the low pressure zone to dominate in this region. Future CFD analysis and cold-flow testing will examine the effects of secondary port placement near the end of the spike where the pressure defect behind the port will have little area to act upon. When properly designed the fluid mechanical mechanisms should serve as an overall force amplifier.

B. Base Bleed CFD Analysis

The nozzle truncation creates a base area on the spike that potentially experiences a pressure somewhat lower than the ambient pressure. This “suction” decreases the overall thrust of the nozzle. If the base area is significant when compared with the overall area of the nozzle, the thrust loss can be substantial. This base pressure effect can be compensated to some degree by allowing for “base bleed” where a small amount of mass flow is ejected from the base of the plug. Figure 8 shows the geometry of the base bleed port included in the test article.

Hot fire and cold-flow test results have shown benefits for a small amount of base-bleed although there is some disagreement on the overall effectiveness of doing so. Additionally, the degree of benefit depends strongly on the ambient pressure.⁹ At low nozzle pressure ratios, the aerospike wake is “open” and the base pressure of the aerospike is nearly equal to ambient pressure. At a point near the design pressure ratio the aerospike wake “closes” and both the base pressure and the pressure along the aerospike surface becomes invariant to external pressure. The effects of base bleed appear to have little effect in the “open” wake condition and the most effect in the regime just after the wake closes. Although the current spike is designed such that ambient pressure only marginally affects the pressure contours along the spike it is still operating in the “open wake” region and the spike base pressure deviates little from ambient pressure even with base bleed.

The CFD calculations verify this result. As fluid exits the base bleed port the flow immediately separates at the ejection point and does little to increase the base pressure except creating only a slight reduction in the separated base area. It is possible that in a hot-gas reacting flow, however; the injected fluid (either fuel or oxidizer) can be made to burn externally. Heiser and Pratt¹⁰ present data showing that this external burning will significantly

1
2
3 increase the base pressure, and has the potential to significantly augment the total spike thrust level, possibly even in
4 the “open wake” flow condition. The base bleed port is being carried in the design for the cold-flow tests to facilitate
5 traceability for future hot-gas testing.
6

7 8 **V. Static Thrust Stand and Feed System Overview**

9 The following sections discuss the design, fabrication, and calibration of the test apparatus used to perform the
10 static thrust and thrust-vectoring tests. All aerospike static tests were performed in the Engineering Technology
11 Department’s Jet Engine Test Cell on the Utah State University (USU) campus. For static thrust tests, commercially
12 available test stands were examined and found to be excessively expensive and have structural support mechanisms
13 that were unsuitable for mounting the aerospike prototype. Consequently, a custom-made, portable test stand was
14 designed and built to support the needs of the Aerospike project.

15 The test stand features a six-degree-of-freedom load balance, a traversing exit plume Pitot-probe, four plenum
16 pressure transducers, and four plenum thermocouples for flow temperature measurements. Additional flow path
17 pressure and temperature sensors were also included in the test stand. These additional sensors will be described
18 later in the “Propellant Feed System” sub-section. Figure 12 shows overview of the test cart with many of the
19 features itemized. Three axial and three lateral load cells are incorporated into the stand for the force and moment
20 measurements. Based on the orientation of their sensing axes, the six load cells are divided into axial [*Aa*, *Ba*, *Ca*]
21 and lateral [*Al*, *Bl*, *Cl*] groups.
22

23 The thrust stand coordinate system, pictured in , is defined with x-axis vertically upward along the axial
24 centerline of the nozzle. The thrust thus acts along the negative x-direction. The y-axis runs perpendicular to and
25 intersects the longitudinal axis of the axial load cell, *Aa*. The z-axis completes the orthogonal triad. A rotational
26 moment about the y-axis is equivalent to a positive pitching moment; a moment about the z-axis is equivalent to a
27 positive yawing moment; and a moment about the x-axis is equivalent to a positive rolling moment. The origin of
28 the coordinate system is centered in the plane of the plenum mounts, and lies along the sensing axes of the lateral
29 load cells. The thrust stand is designed so that the nozzle exhaust plume exits vertically, and the thrust acts
30 downward into the test cart. Thus positive thrust corresponds to a compressive (negative) load on the axial load
31 cells.

32 Axial loads are sensed with three Omegadyne® model LCCD-100 load cells, while lateral loads are sensed with
33 Omegadyne LCCA-25 load cells. The stagnation pressure from the Pitot-probe was sensed with a 0-30 psia absolute
34 Omegadyne PX-142 pressure transducer. The plenum pressure transducers are manufactured by Omega and have a
35 0-150 psig operating range. The temperatures are sensed by Omegadyne Type-K wire bead thermocouples. A
36 National Instruments® NIcDAQ-9174 Universal Serial Bus multifunction control and data acquisition chassis was
37 used to acquire the data, and to control the various valves associated with initiating the test sequence. A laptop
38 computer running NI Labview 9.0 software was used to capture, synchronize, process, and log data from the load
39 cells, pressure transducers, thermocouples, and initiate the test sequence. Relevant manufacturer’s specifications for
40 operating range and accuracy for each of these instruments are listed in Table 4.
41

42 **A. Traversing Pitot Probe Description**

43 The traversing probe pictured in Fig. 13, is designed to sweep across the aerospike plume centerline. Since the
44 aerospike nozzle compensates so that the exit pressure departs at the local ambient pressure, a separate plume static
45 pressure measurement is not needed. The local ambient pressure is measured using the pre and post-test, zero-flow
46 tare readings from the Pitot-probe transducer. The probe total pressure measurements provide two-dimensional
47 stagnation pressure, Mach number, and mass flow distribution profiles very near the nozzle exit plane. A single axis
48 position controller, mounted on a rack and pinion tracking system was used as the drive mechanism. Figure 14
49 shows this drive mechanism. A 5-watt motor is mounted on top of the traversing block. The motor gears mesh with
50 two large external gears that carry the motor torque down into a shaft inside the block. The shaft has teeth against
51 the track. As the shaft rotates the mount moves. Linear position along the track is sensed by a ThinPot® linear
52 potentiometer. This sensor is constructed from a polyester substrate mounted with pressure sensitive adhesive. The
53 contact wiper applies pressure as it moves with the mount, giving a change in resistance of the linear potentiometer.
54 A commercial H-bridge circuit is used to control the direction and traverse speed of the probe.
55
56
57
58
59
60

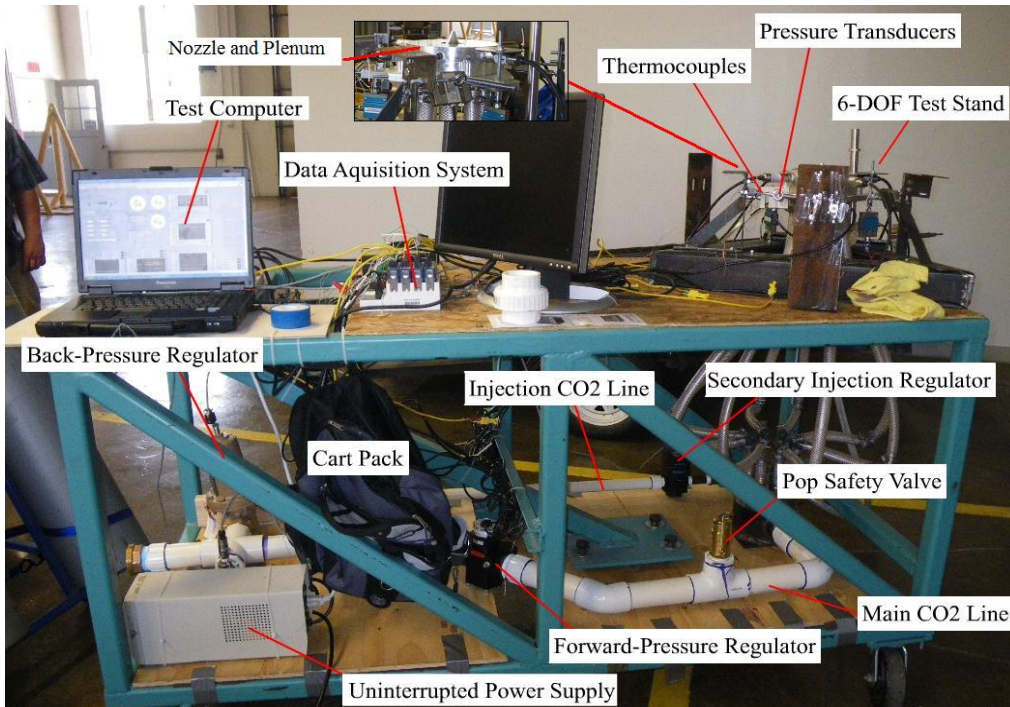


Figure 12. Overview of aerospike thrust stand.

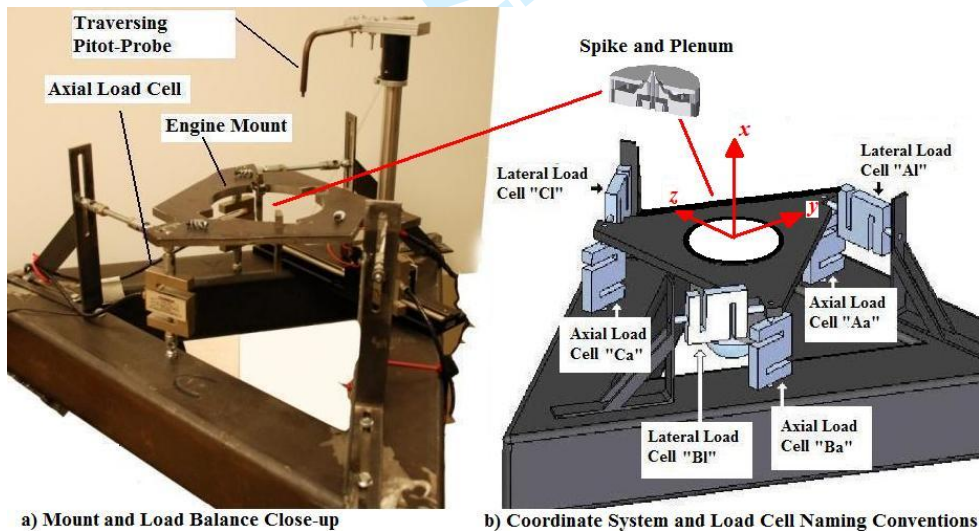


Figure 13. Close-up of aerospike thrust stand and load balance.

1
2
3
4
5
6
7
8
9
10
11
12
13
14
15
16
17
18
19
20
21
22
23
24
25
26
27
28
29
30
31
32
33
34
35
36
37
38
39
40
41
42
43
44
45
46
47
48
49
50
51
52
53
54
55
56
57
58
59
60

Table 4. Manufacturer specifications for thrust stand instrumentation.

Instrument Model	Operating Range	Accuracy
LCCA-25 (<i>Lateral Loads</i>)	±25 lbf (+111:2N)	±0.037% of Full Scale
LCCD-100 (<i>Axial Loads</i>)	±100 lbf (+444:8N)	±0.25% of Full Scale
PX142-030A5V (<i>Nozzle Wake Stagnation Pressure</i>)	0-30 psi absolute (207.0 kPa)	±0.15% of Full Scale
Omega PX409 (<i>Plenum Pressures</i>)	0-1034 kPa gauge (0-150 psig)	±0.5 % of Full Scale
PX142-015A5V (<i>Nozzle Exit Static Pressure</i>)	0-15 psi absolute (103.5 kPa)	±0.15% of Full Scale
Type “K” Wire bead Thermocouple (<i>Plenum Flow Temperature</i>)	-270 to 1372 °C	± 2.2 °C
USB Multifunction Chassis, NIcDAQ-9174	N/A	N/A
16-CH Thermocouple Module, NI 9213	±78.125 mV	24-Bit Resolution
32-CH Analog Input Module, NI 9205	±200 mV	±157 μV, 16-Bit Resolution
16-CH Analog Output Module, NI 9264	±10 V	±0.01 V, 12-Bit Resolution
8-CH Relay, NI 9485		N/A

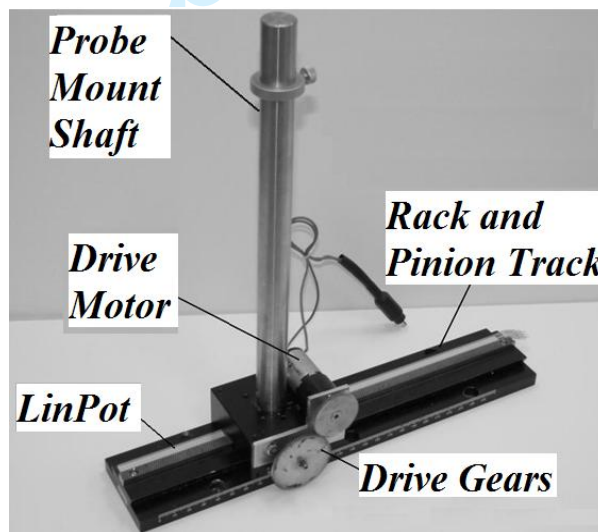


Figure 14. Pitot-probe drive mechanism.

B. Thrust Stand Calibration Procedure

Because of the geometric complexity of the test stand, the entire test stand was calibrated for output forces and moments as a function of the six load cell readings. For this calibration process, the test stand is mathematically modeled as a linear perturbation model of the form

$$\begin{bmatrix} F_x \\ F_y \\ F_z \\ M_x \\ M_y \\ M_z \end{bmatrix} = \begin{bmatrix} \frac{\partial F_x}{\partial V_{Aa}} & \frac{\partial F_x}{\partial V_{Ba}} & \frac{\partial F_x}{\partial V_{Ca}} & \frac{\partial F_x}{\partial V_{Al}} & \frac{\partial F_x}{\partial V_{Bl}} & \frac{\partial F_x}{\partial V_{Cl}} \\ \frac{\partial F_y}{\partial V_{Aa}} & \frac{\partial F_y}{\partial V_{Ba}} & \frac{\partial F_y}{\partial V_{Ca}} & \frac{\partial F_y}{\partial V_{Al}} & \frac{\partial F_y}{\partial V_{Bl}} & \frac{\partial F_y}{\partial V_{Cl}} \\ \frac{\partial F_z}{\partial V_{Aa}} & \frac{\partial F_z}{\partial V_{Ba}} & \frac{\partial F_z}{\partial V_{Ca}} & \frac{\partial F_z}{\partial V_{Al}} & \frac{\partial F_z}{\partial V_{Bl}} & \frac{\partial F_z}{\partial V_{Cl}} \\ \frac{\partial M_x}{\partial V_{Aa}} & \frac{\partial M_x}{\partial V_{Ba}} & \frac{\partial M_x}{\partial V_{Ca}} & \frac{\partial M_x}{\partial V_{Al}} & \frac{\partial M_x}{\partial V_{Bl}} & \frac{\partial M_x}{\partial V_{Cl}} \\ \frac{\partial M_y}{\partial V_{Aa}} & \frac{\partial M_y}{\partial V_{Ba}} & \frac{\partial M_y}{\partial V_{Ca}} & \frac{\partial M_y}{\partial V_{Al}} & \frac{\partial M_y}{\partial V_{Bl}} & \frac{\partial M_y}{\partial V_{Cl}} \\ \frac{\partial M_z}{\partial V_{Aa}} & \frac{\partial M_z}{\partial V_{Ba}} & \frac{\partial M_z}{\partial V_{Ca}} & \frac{\partial M_z}{\partial V_{Al}} & \frac{\partial M_z}{\partial V_{Bl}} & \frac{\partial M_z}{\partial V_{Cl}} \end{bmatrix} \begin{bmatrix} V_{Aa} \\ V_{Ba} \\ V_{Ca} \\ V_{Al} \\ V_{Bl} \\ V_{Cl} \end{bmatrix} \quad (1)$$

In Eq. (1) the vector $[F_x, F_y, F_z, M_x, M_y, M_z]$ is the compendium of the desired forces and moments and the vector $[V_{Aa}, V_{Ba}, V_{Ca}, V_{Al}, V_{Bl}, V_{Cl}]$ is comprised of the output voltages from the six axial and lateral load cells as pictured in Fig. 13. The linear system of Eq. (1) assumes that the voltage readings for the six load sensors have been adjusted so that zero-load on the thrust stand produces zero load cell output. The 36 elements of the Jacobian matrix define the externally applied forces and moments in terms of the sensed (and zeroed) load cell outputs. The calibration procedure reverses the process with multiple known external forces and moments applied to the thrust stand. The corresponding sensor readings are logged. Assuming a set of N calibration inputs \tilde{F} , and a corresponding set of sensor outputs \tilde{V} , where

$$\tilde{F} = \left\{ \begin{bmatrix} F_x \\ F_y \\ F_z \\ M_x \\ M_y \\ M_z \end{bmatrix}_1, \begin{bmatrix} F_x \\ F_y \\ F_z \\ M_x \\ M_y \\ M_z \end{bmatrix}_2, \dots, \begin{bmatrix} F_x \\ F_y \\ F_z \\ M_x \\ M_y \\ M_z \end{bmatrix}_N \right\} \text{ and } \tilde{V} = \left\{ \begin{bmatrix} V_{Aa} \\ V_{Ba} \\ V_{Ca} \\ V_{Al} \\ V_{Bl} \\ V_{Cl} \end{bmatrix}_1, \begin{bmatrix} V_{Aa} \\ V_{Ba} \\ V_{Ca} \\ V_{Al} \\ V_{Bl} \\ V_{Cl} \end{bmatrix}_2, \dots, \begin{bmatrix} V_{Aa} \\ V_{Ba} \\ V_{Ca} \\ V_{Al} \\ V_{Bl} \\ V_{Cl} \end{bmatrix}_N \right\}, \quad (2)$$

then Eq. (1) can be written as the $6 \times N$ dimensional matrix equation,

$$\tilde{F} = J \tilde{V} \quad (3)$$

where J is the Jacobian matrix from Eq. (1). Post-multiplying both sides of Eq. (3) by \tilde{V}^T results in the $6 \times N$ dimensioned system

$$\tilde{F} \tilde{V}^T = J (\tilde{V} \tilde{V}^T) \quad (4)$$

Post multiplying both sides by $(\tilde{V} \tilde{V}^T)^{-1}$ gives the least squares estimate for the Jacobian matrix

$$\hat{J} = \tilde{F} \tilde{V}^T (\tilde{V} \tilde{V}^T)^{-1} \quad (5)$$

The resulting matrix \hat{J} , is the linearized system calibration. Given an arbitrary set of load cell readings (zeroed for the no-load case), the force and moment outputs from the thrust stand can be calculated by substituting the calibration matrix for the Jacobian matrix in Eq. (1). In the calibration procedure, known loads and moments are applied to the test stand using calibration weighting. Three axial and three lateral loads are applied at any one time, and the resulting forces and moments are calculated using the known input geometry. The axial calibration weights are placed over 12.7 mm (1/2 in) diameter steel alignment rods which are approximately 18 in (0.46 m) in length. These rods are threaded onto the same threaded rod that holds the corresponding axial load cell to the engine mounting plate. The masses of these rods are included as part of the calibration load. The lateral calibration loads are applied by weights suspended on lines routed through pulleys and attached to the engine mounting plate.

Figure 15 shows the locations of the weights and pulleys used to apply the calibration inputs to the test stand. In a typical calibration procedure system zeroes are calculated by reading the load cell voltages for 10 seconds with no loads applied and averaging the results for each load cell. These zeroes are analytically removed from the load cell voltage readings. Next, alignment rods are threaded onto each of the axial calibration load points. Each rod has a mass of approximately 0.8 kg (1.7 lb). Next, 3.0 kg (6.6 lbf) masses are placed on each of the rods. This arrangement creates a total axial force of approximately 110.8 N (24.9 lbf). A 0.45 kg (1.0 lbf) mass is subsequently placed on the axial rod above load cell "Aa". The six load cell voltages and reference loads are logged. The 0.45 kg mass is sequentially moved to the axial rods above load cell "Ba," and then load cell "Ca.". Voltages and loads are logged in each case. Next, a 0.57 kg (1.25 lbf) mass is applied to lateral calibration load point "A" through pulley "A". Data are logged and the process is repeated for lateral calibration points "B" and "C." The applied weights are sequentially increased to generate the calibration data set.

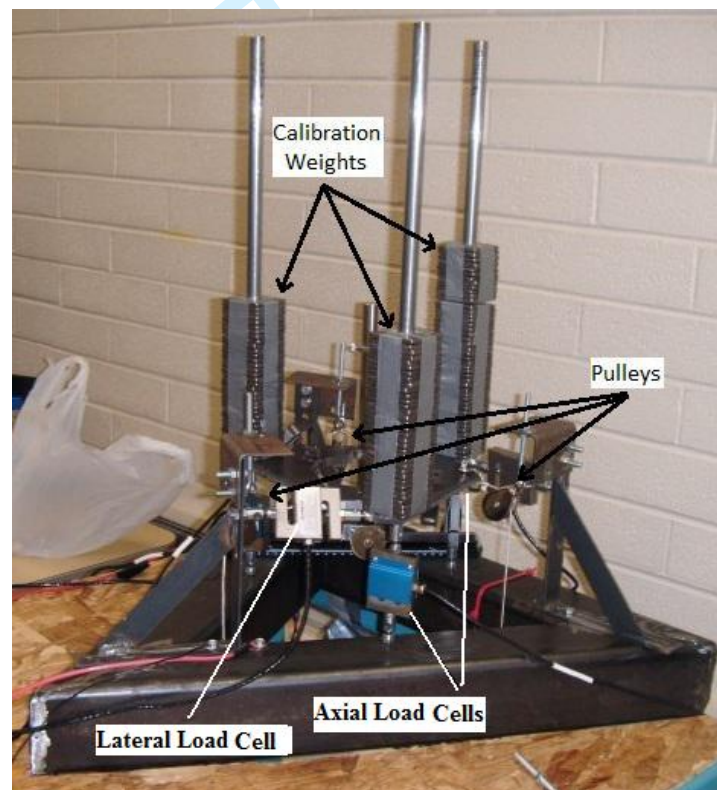


Figure 15. Apparatus used to apply calibration inputs to thrust stand.

Table 5 shows a typical calibration matrix generated using this procedure. The rows of this matrix represent the sensitivity of the output loads and moments to the individual load cell millivolt readings, with rows 1-3 corresponding to F_x , F_y , and F_z , and rows 4-6 corresponding to M_x , M_y , and M_z . Notice that the matrix is not particularly sparse, indicating that all of the sensed loads on the load cells contribute to the over-all load and moment calculations.

Table 5. Typical aerospike test stand calibration matrix

-14806.0236	-15058.9246	-15526.6969	-411.71890	-890.7967	-837.6023
38.5345	-890.1487	935.5346	-404.1727	-3137.2754	3390.6717
-663.4781	440.6172	327.8234	-3815.9789	2124.6036	1865.7721
-74.41130	-134.8726	-150.7640	-470.5827	-531.5757	-539.3858
-27.1716	1899.0908	-1778.5431	-22.6189	-3.9264	-23.6677
2063.5040	-1005.05431	-1046.5082	14.7288	25.2133	20.8681

Table 6 shows the normalized sensitivity of each load or moment to the individual load cell outputs. The values in this table were calculated for each row by taking the maximum absolute value of the six elements in the row, and dividing this value back into the element of the row. The magnitudes show the relative contribution of the load cell output to the force or moment calculation. For example, the major contributors to the yawing moment calculation, M_x (row (3)), are the lateral load cell outputs (columns 4-6). Conversely, the pitching moment calculation M_y , is most sensitive to the output from the axial load cells "B" and "C," and is almost completely insensitive to the outputs from the lateral load cells. As expected, the thrust ($-F_x$) is most sensitive to the outputs from the axial load cells, and almost completely insensitive to the lateral load cell outputs.

Table 6. Typical aerospike test stand calibration, normalized sensitivity.

	<i>Load Cell</i> <i>Aa</i>	<i>Load Cell</i> <i>Ba</i>	<i>Load Cell</i> <i>Ca</i>	<i>Load Cell</i> <i>Al</i>	<i>Load Cell</i> <i>Bl</i>	<i>Load Cell</i> <i>Cl</i>
F_x	0.954	0.970	1.000	0.027	0.057	0.054
F_y	0.011	0.263	0.276	0.119	0.925	1.000
F_z	0.174	0.115	0.086	1.000	0.557	0.489
M_x	0.138	0.250	0.280	0.872	0.986	1.000
M_y	0.014	1.000	0.937	0.012	0.002	0.012
M_z	1.000	0.487	0.507	0.007	0.012	0.010

C. Calibration Uncertainty Estimates

A total of 32 independent calibration data sets were generated. Collectively these data were used to calculate the calibration matrix for the system. Four of these load cases imparted identical forces and moments to the test stand and were used to estimate the statistical uncertainty of the calibration.

Table 7 shows the statistical results from the four identical load cases. These data are used to estimate the accuracy of the test stand measurements.

Table 7. Statistical evaluation of four identical load calibration cases.

	$F_x(N)$	$F_y(N)$	$F_z(N)$	$M_x(N-m)$	$M_y(N-m)$	$M_z(N-m)$
Applied Load	-10.5564	9.2343	-146.2732	1.5795	1.3984	-0.7730
<i>Case 1</i>	-10.4109	8.7975	-144.8075	1.5504	1.3641	-0.7144
<i>Case 2</i>	-10.0210	8.8739	-145.2573	1.5906	1.4094	-0.7168
<i>Case 3</i>	-10.2296	9.1023	-147.0431	1.7030	1.4112	-0.7285
<i>Case 4</i>	-10.0759	9.0838	-144.6441	1.7964	1.3039	-0.7290
Mean	-10.1844	8.9644	-145.4380	1.6601	1.3722	-0.7222
Standard Deviation	0.1749	0.1520	1.1010	0.1115	0.0504	0.0077
Error	0.3721	-0.2700	0.8352	0.0806	-0.0263	0.0108
Error (%)	3.65%	3.01%	0.57%	4.86%	1.91%	1.50%

When these sample statistics are used to approximate the 95% confidence interval on the mean error estimate using the confidence interval formula,¹¹

$$S_{\bar{x}} = t_{95} \cdot \hat{\sigma}_x / \sqrt{N} \quad (6)$$

In Eq. (6) $S_{\bar{x}}$ is the mean error confidence level, $\hat{\sigma}_x$ is the sample standard deviation, and t_{95} is the t-distribution variable corresponding to a 0.95 double-ended probability corresponding and N-1 degrees of freedom. For this case, as shown in

Table 7, $t_{95}=3.19$ and $N=4$. These intervals are shown in column 2 of Table 8. The mean error is a systematic error and is subtracted from the results of calculations from Eq. (13). The confidence interval is the random uncertainty in the test-stand measurements.

Table 8. Test stand mean measurement error uncertainty estimates.

Measurement	Mean Error \pm Confidence Interval	Total Measurement Uncertainty Estimate
$F_x (N)$	0.372 + 0.278	+0.279 N (+2.64%)
$F_y (N)$	-0.270 + 0.242	+0.242 N (+2.62%)
$F_z (N)$	0.835 + 1.752	+1.752 N (+1.2%)
$M_x (N\cdot m)$	0.081 + 0.177	+0.177 N-m (+11.23%)
$M_y (N\cdot m)$	-0.263 + 0.080	+0.082 N-m (+5.83%)
$M_z (N\cdot m)$	0.108 + 0.012	+0.020 N-m (+2.59%)

The calibration weights were initially measured using a Weighmax W-C03 digital scale. The scale measurement uncertainty, based on manufacturer specifications, is +0.005 kgf. The uncertainty in the moment-arm points on the lateral load cells is estimated at 1.6 mm (1/16th inch). Factoring in the uncertainty in the scale measurements and moment arm measurements as systematic errors and then root sum-squaring these errors with the random uncertainties from column 2 of Table 8, the total estimated test stand measurement uncertainty was calculated. These total measurement uncertainty estimates are listed in column 3 of Table 8.

D. Propellant Feed System

Figure 16 presents a schematic diagram of the associated cold-gas feed system. Saturated liquid carbon dioxide is stored in standard K-sized storage tanks, with each tank having a storage capacity of approximately 25 kgs. Multiple tanks were manifolded to assure that the required mass flow levels and run times can be achieved. Flow out of the tanks is controlled via a pneumatic ball valve. The pneumatic valve actuator is controlled with a 12-volt Direct Current (DC) solenoid valve. Beyond the ball valve, carbon dioxide flows into an expansion tank that drops the pressure from the saturation pressure of carbon dioxide, 4825-5515 kPa (700-800 psia) at room temperature, to approximately 1035 kPa (150 psi). The downstream pressure is controlled using a back-flow pressure regulator and a primary regulator in parallel to drop the plenum feed pressure to approximately 690 kPa (100 psi) at the plenum inlet.

At full pressure, the primary regulator is sized to allow one kilogram per second mass flow and the back-flow regulator starts at approximately half that value. As the tanks evacuate and the overall system pressure drops, flow through the back-pressure regulator diminishes to zero. Thermocouples and pressure transducers are used to monitor the temperature and pressure, and to estimate the flow rates in the feed system. An additional electronic regulator in parallel with the main flow regulator controls the upstream pressure of the secondary (thrust vectoring and base-bleed) flow injection ports. Figure 17 shows the multiple tanks on the propellant cart, along with the expansion tanks and the test initiation ball valve.

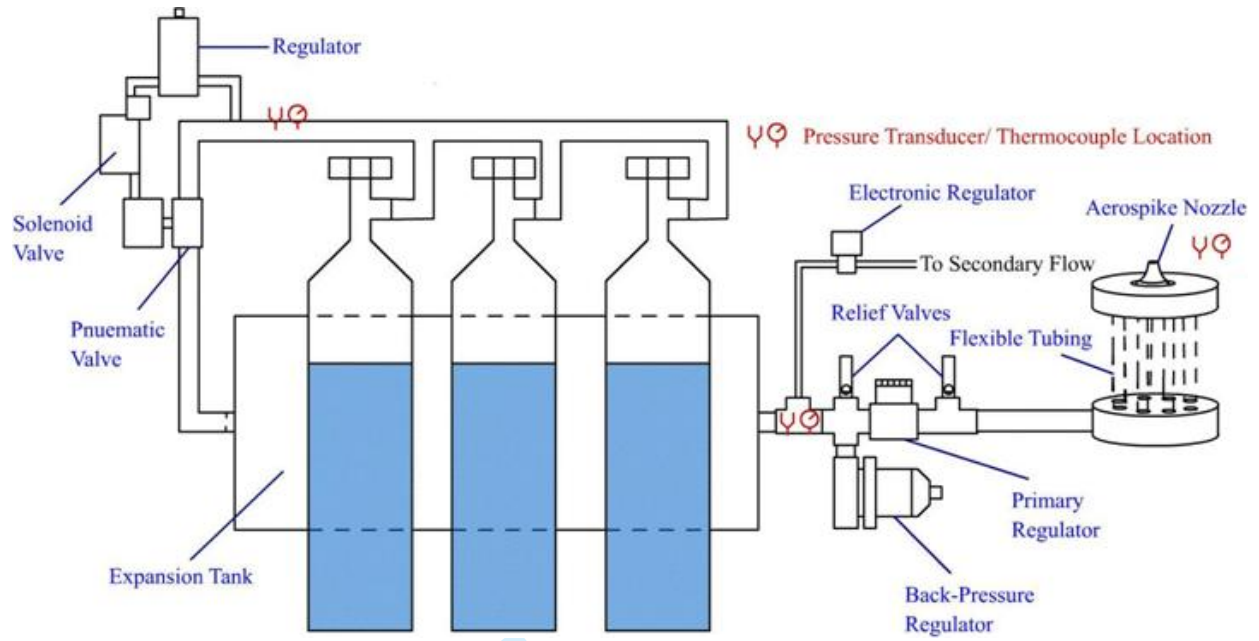


Figure 16. Aerospike propellant feed system.

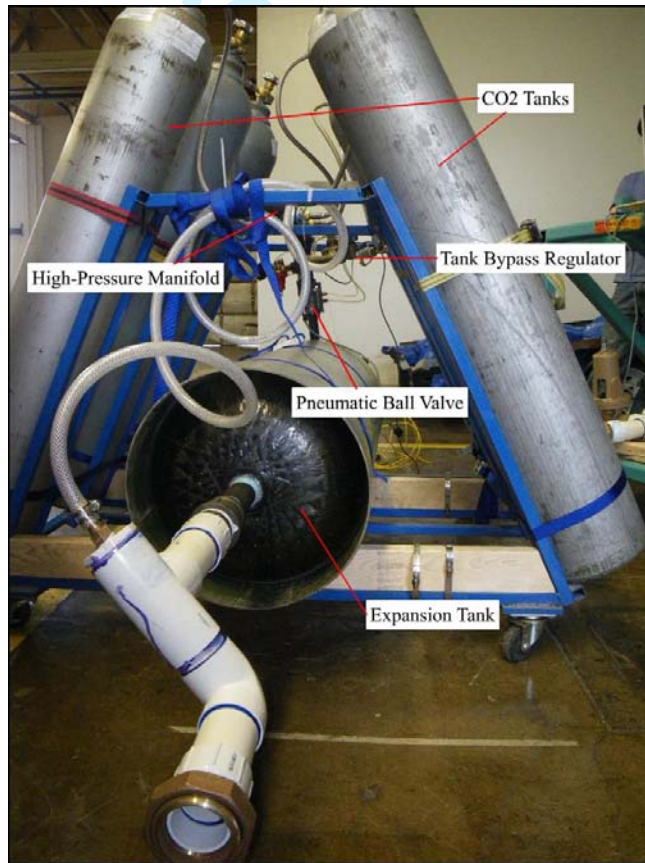


Figure 17. Propellant (CO₂) storage cart with expansion tank.

1
2
3
4
5
6
7
8
9
10
11
12
13
14
15
16
17
18
19
20
21
22
23
24
25
26
27
28
29
30
31
32
33
34
35
36
37
38
39
40
41
42
43
44
45
46
47
48
49
50
51
52
53
54
55
56
57
58
59
60

VI. Preliminary Test Results

In total, four tests of the aerospike systems were completed. The first two tests were merely “shakedown” runs where the functionality of the test apparatus was verified. Results from the two subsequent data-gathering tests are presented here.

A. Axial-Force and Plenum Flow Properties

Figure 18 presents the axial-force (thrust) and plenum flow properties from these two tests. For the first data run (*Test 3*) the primary pressure regulator “set” pressure was higher than the achieved plenum pressure, thus the regulator was unable to regulate the flow. Consequently, the plenum pressure changed continuously during the run. For the second run (*Test 4*) the regulator set pressure was dialed down, and produced a substantially more level plenum pressure. The lower regulator set-pressure resulted in a slightly lower thrust. The measured thrust, shown in Fig. 18a, is lower than the original design thrust of approximately 450 N (Table 2). This difference is primarily a result of lower than anticipated orifice sizes in the propellant storage cylinders, resulting in much lower than expected pressures upstream of the expansion tank choking orifice. The original aerospike design assumed an operating plenum pressure of 775 kPa; however the achieved plenum pressure, shown in 18b, is approximately 600 kPa. When measured thrust for these actual plenum pressures are compared with the predicted thrust for a 600 kPa plenum pressure (Table 2), the actual thrust levels are low by less than 10%.

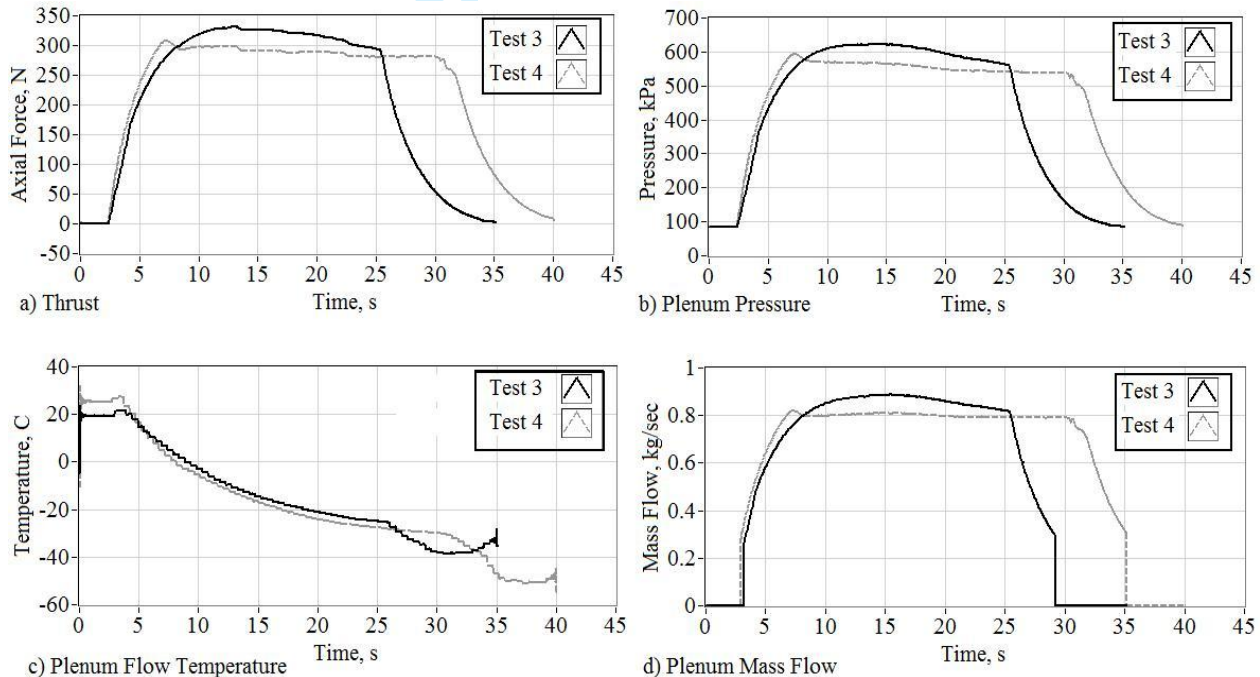


Figure 18. Axial force (thrust) and plenum flow properties.

The fluid temperature in the main plenum, plotted in Fig. 18c, drops dramatically as the tanks evacuate. For the unregulated flow case (*Test 3*), this temperature drop significantly affects the mass flow rate through the system. For the successfully regulated flow case (*Test 4*) the system mass flow remained significantly more constant throughout the entire test. Figure 18d presents these mass flow comparisons. The initial minor temperature rise observed in both cases is attributable to the air trapped in the system being compressed before the CO₂ fills the entire system volume.

B. Lateral-Force and Secondary Injection Flow Properties

For each of the above tests, there were two secondary injection (thrust-vectoring) pressure-pulses. Each pulse was approximately five seconds in duration. Figure 19 shows the resulting lateral forces, and the secondary injector flow properties. Because the mass flows, plotted in Fig. 19d, are considerably smaller; the secondary flow temperature, depicted in Fig. 19c, does not drop nearly as dramatically as does the main plenum flow. The injected

flow pulses, plotted in Fig. 19b, are very effective at producing side forces; and the resulting force outputs are crisp and reproduce the input pulses with a high degree of fidelity. The achieved side force levels are approximately 1.5% of the total thrust level.

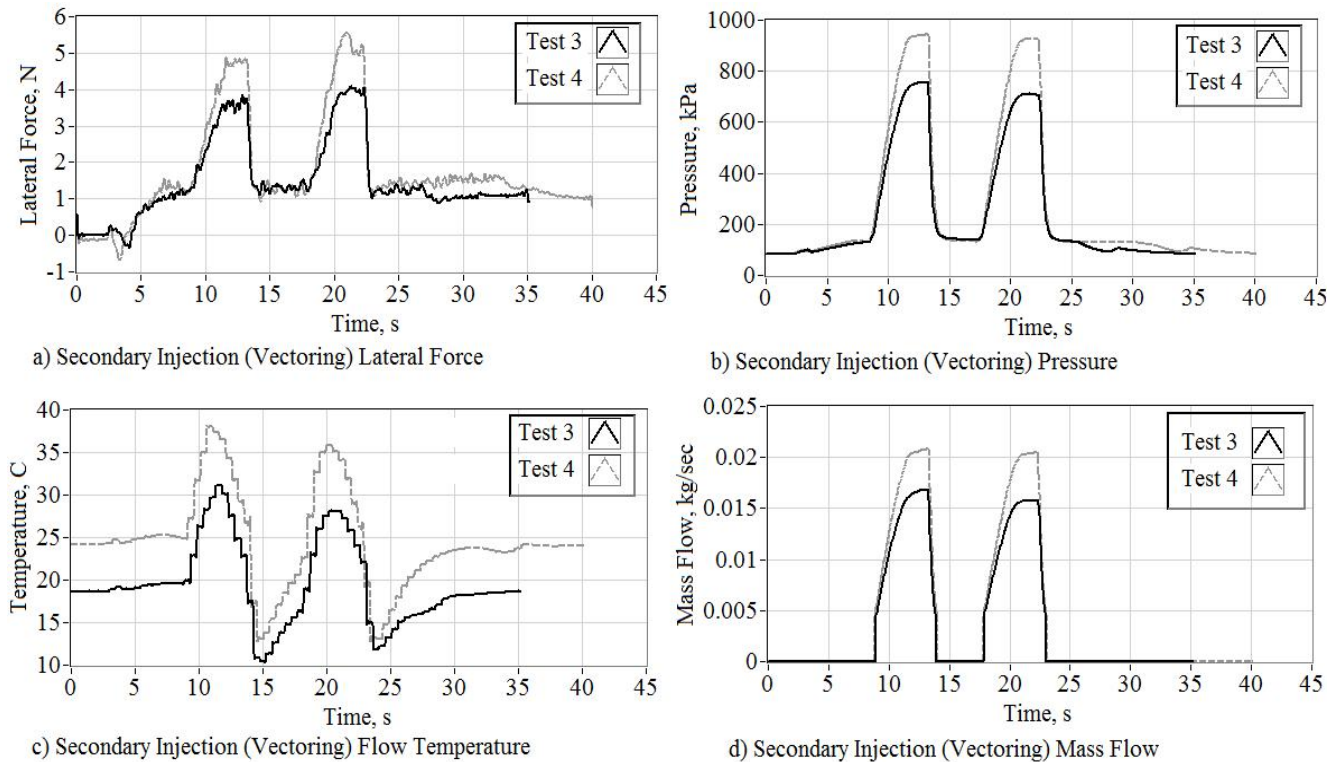


Figure 19. Lateral force (thrust vectoring) and secondary-injection flow properties.

C. Thrust Vectoring Effectiveness of Secondary Flow Injection

To assess the effectiveness of the injection mechanism and the current port placement on the aerospike nozzle, control tests were performed with only the secondary injection flow active. These test cases benchmark the reaction-momentum thrust achieved by the secondary injection without the surface fluid interactions. Figure 20 presents results for a typical “injector only” stand-alone test. The generated side-force Fig. 20a, secondary flow injection pressure (Fig. 20b), and mass flow (Fig. 20c), taken from Fig. 18 are compared to the results for the “injection only” flow tests. For this control case the side force effectiveness of the secondary flow is slightly larger than the force produced for both tests when the full main plenum flow was active. This result occurs even though the pulse-pressure and secondary mass flow lies between the levels of the two tests performed with the plenum flow active.

Figure 19d shows another comparison where the side-force specific impulses, defined by

$$I_{sp_{sf}} = \frac{F_y}{g_0 \cdot \dot{m}_{\text{secondary injection}}} \quad (7)$$

are compared for tests 3 and 4 and the stand-alone injection only tests. The side-force specific impulses for the injection-only tests are moderately higher than the side-force values from tests 3 and 4 with the full plenum mass flow. This result suggests that the local fluid interactions on the surface of the plug produce a localized flow expansion that actually reduces momentum thrust of the injected fluid. This provides confirmation of the previously discussed CFD analysis which suggested that the flow phenomenon upstream and downstream of the injection port

would have competing influence on the overall magnitude of the side force. Thus the desired amplification effect was not achieved. For reference purposes the axial (plenum flow) specific impulses *from tests 3 and 4*, defined by

$$I_{sp\ axial} = \frac{F_x}{g_0 \cdot \dot{m}_{plenum}} \quad (8)$$

are also plotted on Fig. 19d. The axial-thrust specific impulse values are within 2-3% of the predicted values presented in Table 2 for the 600 kpa chamber pressure. Both side-force specific impulses are significantly lower than the main-flow axial I_{sp} values from tests 3 and 4. There are two reasons for this lower efficiency; 1) The secondary injection jets have sonic exit ports with a 1:1 expansion ratio; whereas the main aerospike flow is expanded by at least 2.47:1 and is supersonic, and 2) The secondary injection ports are machined flush to the spike surface with an aft-facing orientation, and this aft-facing injection angle reduces the overall reaction thrust produced by the jet mass flow.

D. Secondary Injection Deflection of Main Flow Plume

A primary focus of follow-on work will be to examine new port locations or form factors that can achieve the desired aerodynamic enhancement effect. Even though the desired aerodynamic amplification side-force was not achieved with the initial nozzle design, the results are promising. The secondary injection pressures demonstrate the ability to significantly deflect the main flow plume exit angle. The deflection of the aerospike exit plume during the first vectoring test (Test 3 above) clearly appears in the video-capture images shown in Fig. 21. The opaque jet is produced by solidifying carbon dioxide in the nozzle plume. Although this phase change somewhat distorts the effective fluid coefficients, it provides a powerful mechanism for fluid flow visualization. The arrows near the tops of the images show the relative deflection of the plume from one image to the other. The images were taken approximately two seconds apart. The first video image shows the plume position immediately as the secondary flow injection is initiated 18.018 seconds after the ball valve was opened. The second image occurs just before the secondary injection pressure has reached its peak value at 20.020 seconds. The plume angular deflection verifies that the secondary flow injection is modifying the flow field and is not simply acting as a reaction-control.

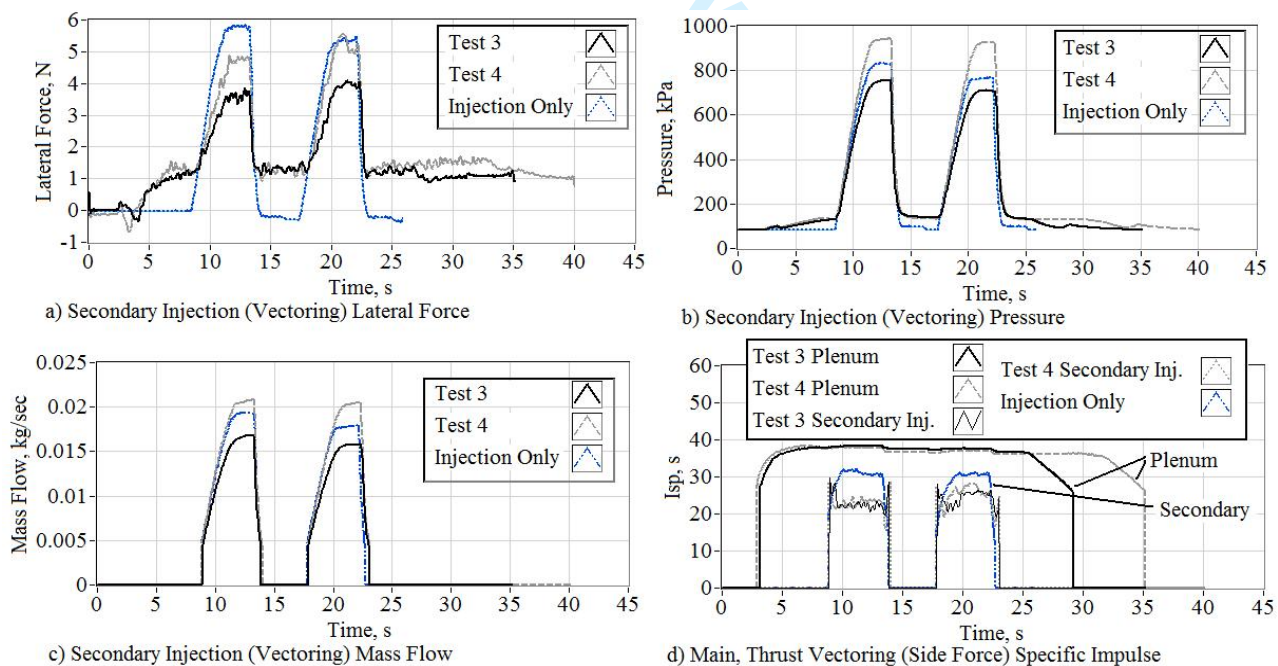


Figure 20. Thrust vectoring effectiveness for stand-alone secondary flow compared to vectoring with main plenum flow active.

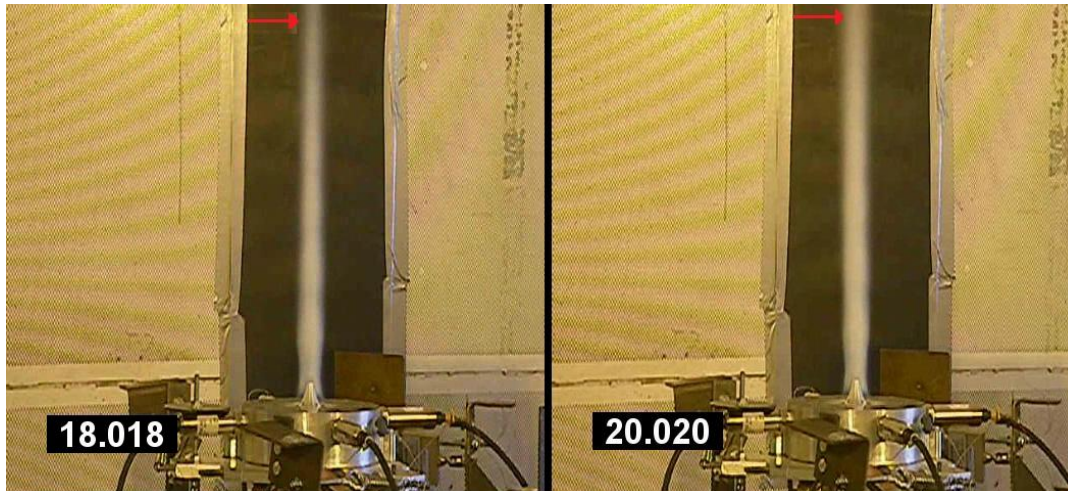


Figure 21. Video-captured images of aerospike plume deflection by secondary flow gas injection.

VII. Conclusion

The fluid mechanics of aerodynamic thrust vectoring on a small scale aerospike nozzle has been the primary focus of the year 1 investigation. Both analytical and experimental investigations have been performed. A six-degree-of-freedom test cell has been designed, fabricated, integrated, calibrated, and used to generate preliminary test data. A series of CFD calculations have been performed, and are compared with test stand results.

To examine the tradeoffs associated with the aerospike design, and to size the system for thrust and mass flow levels that are practical, a parametric study was conducted using conventional inviscid, axi-symmetric compressible fluid mechanics techniques. In a trade study the appropriate test geometry was selected, and these sizing calculations were verified by CFD. These CFD solutions were extended to non axially-symmetric cases to investigate the effectiveness of the secondary flow injection for thrust vectoring. The initial CFD results show the relevant flow phenomenon that must be manipulated to produce the desired size force amplification on aerospike nozzles with gaseous flow injection.

A custom-made, portable, test stand was designed and built to support the needs of the aerospike project. The test stand features a six-degree-of-freedom load balance, a traversing exit plume Pitot-probe, four plenum pressure transducers, and two plenum thermocouples for flow temperature measurements. Because of the geometric complexity of the test stand, the entire test stand was calibrated for output forces and moments as a function of the six load cell readings. Extensive uncertainty analysis was performed to calculate the expected accuracies of the test results. The uncertainty analysis and demonstrated repeatability of thrust vector cold-flow results show that the test apparatus have adequate accuracy fidelity to accomplish the remainder of static testing objectives required by the project.

A total of four tests of the aerospike systems have been completed. The first two tests were merely “shakedown” runs where the functionality of the equipment and software were verified. The following two tests gathered a significant amount of data and demonstrated that the injected flow pulses are effective at producing side forces, and the resulting force outputs are crisp. The input pulses are also reproduced with a high degree of fidelity. The achieved side force levels are approximately 1.5% of the total thrust level. A primary focus of follow-on work will be to examine new port locations or form factors that can achieve side-force amplification factors that conform more closely to thrust vectoring results for current state-of-the-art used in conventional bell nozzles .

References

¹ D. Stephenson, and H. J. Willenberg, Mars Ascent Vehicle Key Elements of a Mars Sample Return Mission, IEEEAC #1009. 2006.

² Bui, T. T., Murray, J. E., Rogers, C. E., Bartel, S., Cesaroni, A., and Denneett, M., "Flight Research of an Aerospoke Nozzle Using High Power Solid Rockets," AIAA Paper 2005-3797, July 2005.

³ Saturn MS-II-1-J-2T-250K, Encyclopedia Astronautica, (retrieved: 21 January 2009).
<http://www.astronautix.com/stages/satt250k.htm>.

⁴ G.S. Mungas, D.J. Fisher, M. Johnson, B. Rishikof, NOFB Monopropellant Propulsion System for Lunar Ascent vehicle Utilizing Plug Nozzle Ascent Engine, Internal Presentation to JSC, With permission from Firestar Engineering, LLC, Nov. 2008.

⁵ Anderson, J. D., Modern Compressible Flow with Historical Perspectives, 3rd ed., McGraw-Hill, New York, 2003, Chap. 11.

⁶ Lee, C., and Thompson, D. D., "Fortran Program for Plug Nozzle Design," NASA TM X-53019, July 1964

⁷ "Flow Modeling Solutions for the Aerospace & Defense Industries, Ansys-Fluent, Inc.,
<http://www.fluent.com/solutions/aerospace/index.htm> [retrieved: 24 June 2010].

⁸ Wu, J., Chapkis, R. L., and Mager, A., "Approximate Analysis of Thrust Vector Control by Fluid Injection," *ARS Journal*; Vol. 31, 1961, pp. 1677-1685

⁹ Wang, C.-H., Liu, Y. and Qin, L.-Z., "Aerospoke nozzle contour design and its performance validation," *Acta Astronautica*, Vol. 64, 2009, pp. 1264-1275

¹⁰ Heiser, W. H., and Pratt, D. T., *Hypersonic Airbreathing Propulsion*, 5th ed., AIAA Education series, American Institute of Aeronautics and Astronautics, Washington, DC, 1994, pp. 455-464.

¹¹ Beckwith, T. G., Marangoni, R. D., and Lienhard V, J. H., *Mechanical Measurements*, 6th Ed., Prentice Hall, 2006, pp.43-73.